Catalysis Science & Technology

Towards the Preparation of Binderless ZSM-5 Zeolite Catalyst: the Crucial Role of Silanol Nest

Journal:	*Catalysis Science & Technology*
Manuscript ID	CY-ART-06-2020-001289.R2
Article Type:	Paper
Date Submitted by the Author:	03-Oct-2020
Complete List of Authors:	li, zaichao; Dalian University of Technology, jiang, xiao; Oak Ridge National Laboratory Xiong, Guang; Dalian University of Technology, nie, binjian; University of Birmingham Liu, Chunyan; State Key Laboratory of Fine Chemicals He, Ning; Dalian University of Technology, State Key Laboratory of Fine Chemicals Liu, Jiaxu; Dalian University of Technology, School of Chemical Engineering

ARTICLE

Towards the Preparation of Binderless ZSM-5 Zeolite Catalyst: The Crucial Role of Silanol Nest

Zaichao Li[a,1], Xiao Jiang[b,1], Guang Xiong[a], Binjian Nie[c], Chunyan Liu[a], Ning He[a], Jiaxu Liu[*a]

Zeolites, containing abundant silanol nests, are often called defective zeolites. Zeolite-based catalysts are shaped to be used effectively in industrial applications. Binders, which are catalytically inert, are indispensable components in the forming process. However, massive amount of binders (usually 30~50 wt.%) may cover the surface of the zeolites, thereby limiting the access to catalytic sites. In the present work, two types of binderless zeolites were prepared by the alkali post-treatment using defective ZSM-5 zeolite as the starting materials, namely monolithic binderless ZSM-5 zeolites dominated by micropores and hierarchical monolithic binderless ZSM-5 zeolites. It has been found that the silica binder can be converted into the zeolite phase in the binderless defective ZSM-5 zeolites. Moreover, the additional aluminum source can be incorporated into zeolitic framework upon alkaline treatment. However, if the zeolite does not contain silanol nests, the Al incorporation is impossible. Combining with various characterization results, we proposed the formation mechanisms of binderless ZSM-5 zeolites, including re-crystallization and alumination. As expected, the as-treated binderless zeolites exhibit higher activity and selectivity than the ordinary shaped zeolite with the binder in the catalytic cracking of *n*-hexane. This work provides new insight into the preparation and optimization of more monolithic zeolite catalysts from practical point of view.

Received 00th January 20xx,
Accepted 00th January 20xx

DOI: 10.1039/x0xx00000x

1. Introduction

Zeolite materials have been widely used in industrial processes such as catalysis, adsorption, and separation due to their outstanding catalytic activity, unique shape-selectivity, and high hydrothermal stability.[1, 2] However, the intrinsic micropores of zeolites usually restrict diffusion of reagents and reaction products, which lead to low activity in reactions, especially involving large molecules.[3-6] Mesoporous or macroporous materials can solve the diffusion problem, but their applications are also limited due to their low hydrothermal stability.[7, 8] In this context, hierarchical zeolites attract growing attention by providing solutions to overcome the diffusion problem due to the combined advantages of superior activity from microporous side and facilitated mass transfer from mesoporous or macroporous sides.[9-13] Most of the investigations on hierarchical porous zeolites focus on the zeolite powder rather than the technical catalyst or multicomponent catalyst body.

In most cases, synthesized zeolites are usually powders, and they suffer from several issues including the difficulty in recycling, purification and critical pressure drop inside the reactor.[14] To overcome these problems, zeolite powders have to be fabricated into shaped forms to obtain a necessary mechanical strength for industrial applications.[15-17] Processes have been developed to shape zeolite powders into macroscopic forms (such as extrudates, pellets, granules, etc.).[18] In the shaping process, the binder, a crucial additive, is employed to agglomerate the components to improve the plasticity of the system, and silica, alumina, and natural clay (kaolin, montmorillonite, bentonite, etc.) are normal choices. In most cases, binders are usually inert components of inorganic oxides with refractory properties. They might cover the surface of the catalyst, thereby limits access to the catalytic sites. What is more, channels within the binder may induce additional diffusional resistance to reactant and product molecules.[19] Therefore, the addition of massive amount of binders (usually 30~50 wt.%) signifies a decline in the proportion of available catalytic active component in catalysts. Recently, Perez-Ramirez, Weckhuysen, and colleagues have studied a series of shaped catalysts with advanced characterization techniques.[20-23] These studies suggest that different types of binders and organic additives can significantly affect the catalytic properties of the catalysts. For example, the accessibility of acid sites in zeolites may be reduced in the shaping process. Nevertheless, such issue from binders is frequently neglected in academic studies, because it is generally qualified as a technical issue.[24] Actually, a solid study of binder effects is of scientific significance to zeolite catalyst from practical point of view.

In the past decades, the preparation of binderless zeolite has

[a] *State Key Laboratory of Fine Chemicals & Department of Catalytic Chemistry and Engineering, Dalian University of Technology, Dalian, 116024, China.* E-mail: liujiaxu@dlut.edu.cn; Tel: +86-411-8498-6162
[b] *Chemical Sciences Division, Oak Ridge National Laboratory, Oak Ridge, TN 37831 USA*
[c] *Birmingham Centre for Energy Storage & School of Chemical Engineering, University of Birmingham, Edgbaston, Birmingham, UK, B15 2TT*
[1] Z.C. Li and X. Jiang contributed equally to this work.
† Electronic Supplementary Information (ESI) available. See DOI: 10.1039/x0xx00000x

been considered a solution to solve the binder problem. Y. Long et al.
have reported that a binder-free ZSM-5 catalyst, prepared by hydrothermal treatment method, exhibits higher activity and longer lifetime in the dehydration of crude methanol to dimethyl ether reaction than binder-containing catalysts.[25] J. Zhou et al. have prepared full-crystalline hierarchical monolithic ZSM-5 zeolites by the steam-assisted method. They have converted the mixture phase of zeolite/binder to the pure zeolite phase and proved its high activity and long lifetime in the Methanol-to-Hydrocarbons (MTH) reaction.[26] The preparation of binderless ZSM-5 by dry gel conversion (DGC) method has been reported by several groups, which uses organic structure-directing agents (OSDA) to assist the transformation of amorphous precursors into ZSM-5 morphology.[27-35] The abovementioned investigations have successfully showed feasibility of preparing binderless zeolite catalysts with solved binder-covering issues. However, the acidity of these binderless zeolite catalysts decreases drastically compared to the original zeolite powder, and remains as an unresolved issue. Indeed, solutions to the binder-covering issues and the parallel preservation of acid centers is rather challenging in the preparation of binderless zeolite catalysts.

The formation of a "hydroxyl-nest defect" over silica-alumina zeolites consisting of 4 silanols, a substitute for [AlO_4] tetrahedron, has been first proposed by Barrer and Makki.[36] The defective MFI zeolites show a high density of silanol nests, with most located in the internal cavities. The silanol nests can provide active sites and space for grafting other atoms. Chang et al. have reported the direct insertion of aluminum into high silica zeolite frameworks, in which the incorporation of Al atoms into tetrahedral framework sites is through a reaction of aluminum halides with silanol nests.[37] This could be a solution to preserve the acid property of the zeolite during the preparation of the binderless zeolite catalysts.

As mentioned above, it is of great importance to avoid the significant losses of diffusion performance and acidic property after the shaping process. In the present work, a ZSM-5 zeolite powder containing abundant silanol nests was used as raw materials to prepare two types of binderless catalysts: the monolithic binderless ZSM-5 zeolites dominated by micropores and the hierarchical monolithic binderless ZSM-5 zeolites. For comparison, commercial ZSM-5 zeolites without silanol nests were used as benchmark. Results show that the acidity of the defective binderless ZSM-5 zeolites can be significantly increased by adding aluminum source during the alkali treatment, whereas such promotional effects on acidity cannot be observed on the binderless commercial ZSM-5 zeolite. Such difference originates from the reaction between the additional aluminum source and silanol nests, through which Al can migrate into the zeolite framework. *n*-Hexane catalytic cracking was used as a probe reaction, and the as-prepared binderless zeolites exhibit higher activity and selectivity of C_2-$C_3^=$ olefins in comparison to zeolite extrude with binder.

2. Experimental

2.1 Catalyst preparation

ZSM-5 zeolites with a SiO_2/Al_2O_3 molar ratio of 107 were supplied by Dalian Ligong Qiwangda Chemical Technology (Dalian, China). Previous study found large amount of silanol hydroxyl groups existed over this sample,[38] named it defective ZSM-5 zeolite. This product was calcined at 540°C for 5 h in air. The obtained white product was labeled as P-D.

P-D (150 g) and binders (125 g, 30% silica sol) were strongly blended at ambient temperature to form a homogeneous mixture, extruded into a uniform body by rapid extrusion molding and then dried at room temperature for 24 h. After that, the product was dried at 110°C overnight. Finally, it was calcined at 540°C for 5 h in air. The product was denoted as E-D.

The binderless defective ZSM-5 zeolites were prepared by employing E-D as precursors. The alkali treatment process was performed in a 50 mL PTFE-lined stainless-steel autoclaves under Tetrapropylammonium hydroxide (TPAOH) solution. E-D (5 g) and TPAOH solution (2.1% aqueous solution, 25 mL) were put into the bottom of PTFE-lined stainless, which was then introduced into an autoclave and heated at 200°C for 24 h. After the washing and filtration steps, the product was dried at 110°C overnight. Finally, the product was calcined at 540°C for 5 h in the air to remove the remained organic template, and the obtained products were labeled as E-D-2.1%T. The exploration of the conditions during the alkali treatment is listed in **Tables S1-S3**.

As a contrast, the Al_2O_3 (74%, 0.03 g) were extra added into a PTFE-lined stainless in the alkali treatment process, and the condition of alkali treatment is the same as E-D-2.1%T. The obtained products were denoted as E-D-2.1%T-Al. The exploration of different aluminum sources during the alumination process is listed in **Fig. S1**. For comparison, E-D (5 g) and TPAOH solution (0.6% aqueous solution, 25 mL) were put into the bottom of PTFE-lined stainless, which was then introduced into an autoclave and heated at 200°C for 24 h. This catalyst has no mesopores and is named E-D-0.6%T. Also, the Al_2O_3 (74%, 0.03 g) were extra added into a PTFE-lined stainless, and the condition of alkali treatment is the same as E-D-0.6%T. The obtained products were denoted as E-D-0.6%T-Al.

Moreover, P-D was also alkali-treated. The condition of alkali treatment is the same as E-D-2.1%T. The obtained white product was denoted as P-D-T. In another contrast, the P-D-T was shaped using a screw extruder, and the condition of extruding is the same as E-D. The product was labeled as P-D-T-E.

Commercial ZSM-5 zeolite with SiO_2/Al_2O_3 molar ratio of 24 was purchased from Zeolyst International to compare with the defective ZSM-5 zeolites. The product was obtained by calcined at 540°C in flowing dry air for 5 h, named as P-C.

P-C (150 g) was vigorously blended and kneaded with binders (125 g, 20% silica sol). The mixtures were then extruded rapidly into uniform cylinders and then dried at room temperature for 24 h. The extrudates were dried at 110°C overnight. Finally, it was calcined at 540°C for 5 h in air. The product was labeled as E-C.

The binderless commercial ZSM-5 zeolites were prepared by the re-crystallization method. In the re-crystallization process, E-C (5 g) and TPAOH solution (2.1% aqueous solution, 25 mL) were put into the bottom of the PTFE-lined stainless, which was then introduced into an autoclave and heated at 200°C for 24 h. After the washing and filtration steps, the product was dried at 110°C for 12 h and then calcined in air at 540°C for 5 h. This sample was denoted E-C-2.1%T.

As a contrast, extra Al_2O_3 (74%, 0.03 g) was added into a PTFE-lined stainless in the re-crystallization process. The condition of re-crystallization is the same as E-C-2.1%T, and the obtained products were denoted as E-C-2.1%T-Al. The SiO_2/Al_2O_3 molar ratio of the four commercial samples is listed in **Table S4**. For clarity, details of above catalysts are summarized in **Table 1** and **Fig. 1**.

2.2 Catalyst characterization

X-ray diffraction (XRD) patterns were recorded using a Rigaku D/max-2004 diffractometer (Rigaku, Kyoto, Japan) with Cu Kα radiation (40 kV, 100 mA) and a 0.01°min^{-1} (2θ) scanning speed.

X-ray fluorescence (XRF) measurements (Bruker, Madison, USA) were obtained with a Bruker SRS3400 spectrometer to determine the bulk silicon to aluminum ratio.

X-ray photoelectron spectroscopy (XPS) studies were carried out on a VG ESCALAB MK2 instrument using Al Kα radiation (1486.6 eV) to estimate the surface silicon to aluminum ratio. The voltage and power are used for the measurements were 12.5 kV and 250 W, respectively. The vacuum in the test chamber during the spectrum collection was maintained at 2×10^{-10} mbar. All binding energies were referenced to the C_1S peak at 284.6 eV of the surface adventitious carbon to correct the shift caused by the charge effect.

TEM and high-angle annular dark field scanning transmission electron microscopy (HAADF-STEM) were done on a FEI (Tecnai F30 G2, The Netherlands) microscopy.

The contents of silica ($Si_{Filtrate}$) and aluminum ($Al_{Filtrate}$) in the filtrate during TPAOH treatment were analyzed by inductively coupled plasma optical emission spectrometry (ICP-OES) using an optima 2000DV instrument.

Nitrogen physisorption was conducted on a Micromeritics ASAP 3020 instrument (Micromeritics, Atlanta, USA) at -196°C to obtain textural information. Before the measurement, the samples (20~40 mesh) were degassed at 350°C for 5 h. The surface area was determined by the Brunauer-Emmett-Teller (BET) methods using the $n(p_0-p)$ vs p/p_0 plot and choose the interval where $n(p_0-p)$ value increases. The micropore and mesopore volume were calculated by the *t*-plot method at P/P_0 of 0.99.

The ammonia temperature-programmed desorption (NH_3-TPD) measurements (Shimadzu, Kyoto, Japan) were employed to investigate the overall acidity of the catalysts. Profiles were carried out on a Quantachrome Chembet 3000 chemisorb instrument. Samples (0.14 g, 20~40 mesh) were loaded into a quartz U reactor and decontaminated with the use of the NH_3-TPD method under helium for 1.0 h; And then, the temperature was cooled down to 150°C for NH_3 adsorption which lasted for 30 min. What is more, physically adsorbed NH_3 was removed by continuous helium purging. Finally, the desorption pattern was recorded from 150 to 600°C in 20 mL/min helium carrier gas. The temperature was increased at a rate of 15 °C·min^{-1}. The amount of acid sites has been quantified and the corresponding results have been provided in **Table S5**.

Fourier transform infrared spectroscopy (FT-IR) was also used to investigate the acidic sites of the catalysts. The spectra for surface hydroxyl (OH) vibrations and pyridine adsorption were recorded with a Nicolet 10 FT-IR spectrometer in the range from 4000 to 400 cm^{-1} with an optical resolution of 4 cm^{-1}. The zeolite samples were pressed into a self-supporting thin wafer (approximately 16 mg) and decontaminated at 400°C under vacuum (10^{-3} Pa) for 4 h in a quartz IR cell equipped with CaF_2 windows. After the pretreatment, the cell was cooled down to room temperature for sample measurement. The hydroxyl vibration spectra were measured by subtracting the background spectrum (recorded with an empty IR cell in the absence of the sample) from the measured sample spectra. The spectra for Pyridine (Py) and 2,6-Di-tert-butylpyridine (DTBPy) were obtained as follows: first, Py or DTBPy adsorption was carried out at 200°C for 5 minutes; second, the evacuation treatment (10^{-3} pa) was conducted for 30 min at 200°C; finally, the spectra were obtained by subtracting the background spectrum (obtained with decontaminated wafers before pyridine adsorption) from the measured spectra. The total amount of Brønsted (C_B) acid sites and Lewis (C_L) acid sites were calculated from the band areas of adsorbed pyridine at 1540 cm^{-1} (1.67 cm/μmol) and 1450 cm^{-1} (2.94 cm/μmol), respectively, using the integrated molar extinction coefficient (IMEC) method.[39]

All solid-state NMR experiments were carried out on an Agilent DD2-500 MHz spectrometer (Agilent Technologies Inc, California, USA). $^1H\rightarrow{}^{29}Si$ CP/MAS NMR experiments were performed with a 4 s repetition time, 4000 scans, and contact time of 1.5 ms. ^{29}Si spectra were referenced to 4,4-dimethyl-4-silapentane sulfonate sodium (DSS).^{27}Al MAS NMR spectra were acquired at 130.2 MHz using a 4 mm MAS NMR probe with 14 kHz spinning speed. The chemical shifts were referenced to 1% Al $(NO_3)_3$ aqueous solutions. The spectra were accumulated for 200 scans with π/12 flip angle of 0.34 μs, and 2 s recycle delay.

2.3 Catalytic performance

The catalytic cracking in *n*-hexane was carried out in a pulse micro-reactor at atmospheric pressure. The reaction was performed at 500, 550, 600, and 650 ℃, respectively. In a typical run, 0.15 g (20~40 mesh) of the catalyst was loaded, then 1μL *n*-hexane was injected into the reactor. Analysis of the composition was conducted on the TECHCOMP GC7900 online gas chromatograph (TECHCOMP, Shanghai, China) equipped with a PLOT-Q column (30 m × 4 mm) and a flame ionization detector.

The *n*-hexane conversion ($C_{n\text{-hexane}}$) and product selectivity (S_i) were calculated by the following equations:

$$C_{n-hexane} = (N_{n-hexane,\,in} - N_{n-hexane,out})/N_{n-hexane,in}$$

$$S_i = \frac{i}{6} * N_i / [N_{n-hexane,in} - N_{n-hexane,out}]$$

$N_{n\text{-hexane,in}}$: amount of *n*-hexane at the inlet; $N_{n\text{-hexane,out}}$: amount of *n*-hexane at the outlet.

Table 1 Properties of the different ZSM-5 zeolites

Sample[a]	Form[a]	Yield (%)	Alkali treatment conditions		
			CTPAOH (%)	Temperature (℃)	Time (h)
P-D[b]	P	—	—	—	—
P-D-T	P	—	2.1	200	24
P-D-T-E (P-D-T + 20% SiO_2 binder)	E	—	—	—	—
E-D (P-D + 20% SiO_2 binder)	E	—	—	—	—
E-D-0.6%T	E	97.8%	0.6	200	24
E-D-0.6%T-Al (E-D-0.6%T + 0.03 g Al_2O_3)	E	96.1%	0.6	200	24
E-D-2.1%T	E	93.4%	2.1	200	24
E-D-2.1%T-Al (E-D-2.1%T + 0.03 g Al_2O_3)	E	92.5%	2.1	200	24
P-C[c]	P	—	—	—	—
E-C (P-C + 20% SiO_2 binder)	E	—	—	—	—
E-C-2.1%T	E	96.4%	2.1	200	24
E-C-2.1%T-Al (E-C-2.1%T + 0.03 g Al_2O_3)	E	95.5%	2.1	200	24

[a] P: Powder, E: Extrudate, T: TPAOH treatment, D: Defective, C: Commercial.
[b] P-D (defective ZSM-5 zeolite powder).
[c] P-C (commercial ZSM-5 zeolite powder).

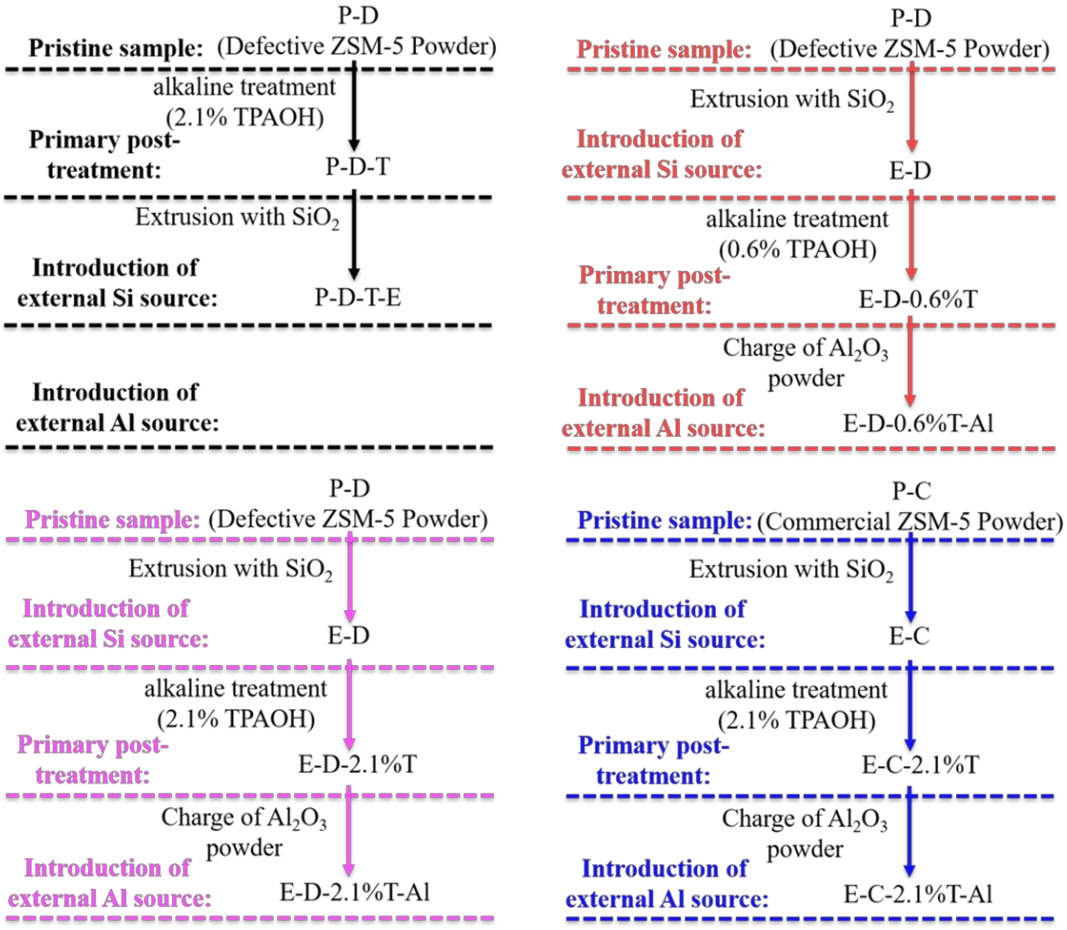

3. Results and Discussion

3.1 Physico-chemical properties of defective ZSM-5 zeolites

Table 2 Physical properties of the different defective ZSM-5 zeolites

Samples	N_2-adsorption results				
	V_{tol}[a] ($cm^3\ g^{-1}$)	V_{micro}[b] ($cm^3\ g^{-1}$)	S_{BET}[c] ($m^2\ g^{-1}$)	S_{micro}[b] ($m^2\ g^{-1}$)	S_{meso}[b] ($m^2\ g^{-1}$)
P-D	0.22	0.11	386	261	125
P-D-T	0.24	0.10	395	225	170
P-D-T-E	0.25	0.08	356	174	182

[a] V_{total} was determined from the amount of N_2 adsorbed at $p/p_0 = 0.99$

[b] *t*-plot method applied to the N_2 isotherm

[c] BET method applied to the N_2 isotherm

To study the effect of hierarchical powder zeolites after shaping, we compared textural properties among P-D, P-D-T, and P-D-T-E. As shown in **Table 2**, the mesopores are successfully increased after the TPAOH treatment, as the surface area of mesopore increases from 125 to 170 $m^2\ g^{-1}$. **Fig. S2** shows N_2 adsorption-desorption isotherms and pore size distributions of the above samples. The isotherm of P-D is identified as Type I which is characteristic of micropores and limited mesopores. The isotherm of P-D-T possesses a typical Type-IV isotherm, suggesting the existence of mesopores. The isotherm of P-D-T-E is identified as a combination of Type I and Type IV with H1 hysteresis loop, indicating the presence of mesopores. The pore distribution of P-D-T-E presents that mesopore volumes are mainly located at the pore size of 4 nm and 6 nm, which are associated with MFI zeolites and the binders, respectively. The formation of mesopores after TPAOH treatment is also corroborated in TEM images in **Fig. 2a**. By contrast, the addition of 20 wt.% SiO_2 binders blocks micropores sharply (**Table 2**), thus limiting the accessibility of acid sites located inside zeolite channels. NH_3-TPD pattern of P-D displays two typical desorption peaks, centered at 230°C and 450 °C. The lower-temperature peak might be associated with weak acid sites and/or weakly adsorbed NH_3 molecules on ammonia cations, while the high-temperature peak corresponds to strong acid sites, respectively. The samples of P-D-T and P-D-T × 0.8 (The forming process used 80% zeolite powder and 20% SiO_2 binder, because the binder is not acidic, so multiply the result of powder by 80%) still displays two pronounced desorption peaks in the NH_3-TPD patterns; Whereas, the desorption peaks, especially the peak associated with the strong acid sites, are significantly reduced for the P-D-T-E. Such reduction in strong acid sites is also reflected from the quantified amounts in **Table S5**. Given the addition of binders, this phenomenon is caused by two reasons: 1) the blockage of micropores limits the accessibility of acid sites located inside zeolite channels; 2) the dilution effect by the addition of 20 wt.% SiO_2 binders dilutes. Compared to the intensities of the desorption peaks of P-D, the reduction in the intensities of those two peaks for P-D-T-E is obviously higher than 20%. Therefore, the dilution effect does not hold a prevailing responsibility for the reduction of the acidities.

Recently, most of the studies on hierarchical porous zeolites focus on zeolite powder, which, however, will cause inevitable losses in micropores and acid sites after shaping hierarchical powder catalysts. Therefore, it is a great challenge to prepare the monolithic multi-stage porous catalyst while preserving its acidity and micropores. To minimize such losses, we treated zeolites with the alkali post-treatment method and compared the various physical and chemical properties of the hierarchical zeolite powder (P-D-T sample) and

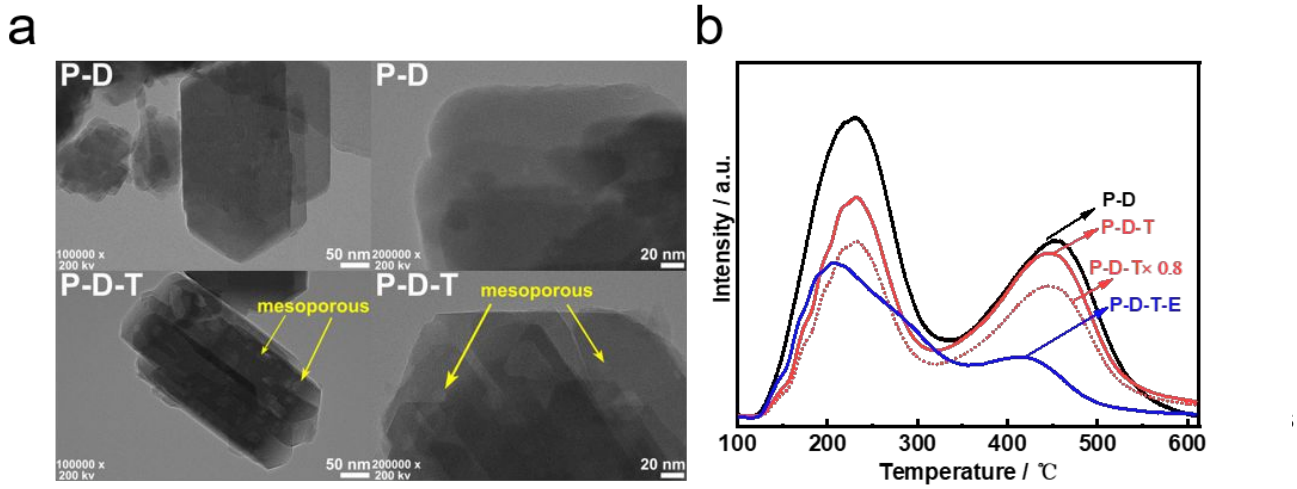

Fig. 2 (a) TEM images and (b) NH_3-TPD profiles of the different defective ZSM-5 zeolites.
P-D (defective ZSM-5 zeolite powder), P-D-T (alkali treatment of P-D), P-D-T-E (Extrudate: P-D-T+20% SiO_2 binder)

monolithic binderless zeolite (E-D-2.1%T-Al sample). As listed in **Table S6**, the pores are almost the same as the original powder, but its acidity has not been completely restored (**Fig. S1**).

Fig. 3 presents XRD patterns of different ZSM-5 samples. Generally, XRD patterns exhibit five diffraction peaks at 7.9°, 8.6°, 23.1°, 23.9°, and 24.3°, which are typical for MFI-type zeolite. Because of the presence of binders, E-D exhibits less-intensive peaks than the other zeolites. Relative crystallinity is then compared and calculated by the areal sum of the five strongest peaks in XRD patterns. If the relative crystallinity of E-D-2.1%T-Al is defined as 100%, the relative crystallinity of different samples can be estimated. As compared in **Fig. 3**, E-D-0.6%T, E-D-0.6%T-Al, E-D-2.1%T, and E-D-2.1%T-Al all have a higher relative crystallinity than E-D, indicating that the silica binders in E-D are converted into zeolite with MFI structure.

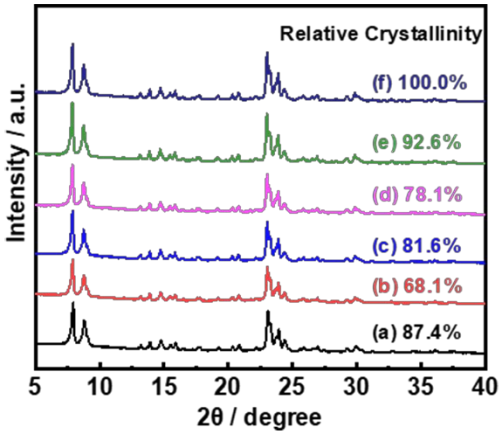

Fig. 3 XRD patterns of the different defective ZSM-5 zeolites.
(a) P-D (defective ZSM-5 zeolite powder), (b) E-D (Extrudate: P-D + 20% SiO_2 binder), (c) E-D-0.6%T (0.6%TPAOH treatment of E-D), (d) E-D-0.6%T-Al (E-D-0.6%T + 0.03 g Al_2O_3), (e) E-D-2.1%T (2.1%TPAOH treatment of E-D), (f) E-D-2.1%T-Al (E-D-2.1%T+ 0.03 g Al_2O_3).

Table 3 Assignments of IR bands

Band (cm^{-1})	Assignment	Ref.
3450	Silanol nest	42
3610	Si(OH)Al	43
3665	Extraframework aluminum hydroxyls	43
3682	Hydrogen-bonded vicinal hydroxyl groups	44
3698	Internal silanol groups free from the structural perturbation	42
3725	Internal silanol groups	44
3741	Isolated silanol hydroxy on the external surface	43

As shown in NH_3-TPD profiles (Fig. 4a), there are two desorption peaks from low to high temperatures, corresponding to weak and strong acid sites, respectively. For E-D, both weak and strong acidity decrease outstandingly after the addition of the silica binder. This result can be explained by the fact that the addition of silica binders dilutes the acid sites of E-D. Moreover, the total acid of E-D-2.1%T slightly increases after TPAOH treatment. This reason can be explained that the case of zeolites extrudates with silica binder, the density of acid sites will be diluted by the binders. Therefore, once the binder crystallized by the addition of TPAOH, the diluent effect will be slightly reduced, leading to the slight increase of acid sites as observed in our case. The acid sites of E-D-2.1%T-Al is clearly recovered compared with E-D, which can originate from additional aluminum sources that transform into Al sites in framework during TPAOH treatment.

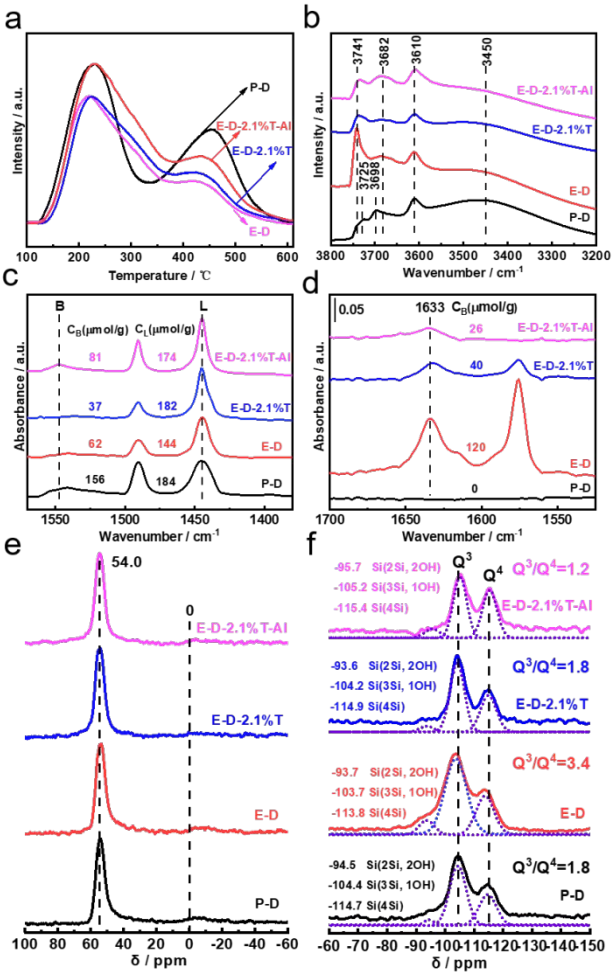

Fig. 4 Properties of the different defective ZSM-5 zeolites.
P-D (defective ZSM-5 zeolite powder), E-D (Extrudate: P-D + 20% SiO_2 binder), E-D-2.1%T (2.1%TPAOH treatment of E-D), E-D-2.1%T-Al (E-D-2.1%T + 0.03 g Al_2O_3).
(a) NH_3-TPD profiles (b) OH-IR spectra (c) Py-IR spectra (d) DTBPy-IR spectra (e) ^{27}Al MAS NMR spectra (f) ^{1}H-^{29}Si CP/MAS NMR spectra.

Zeolites, containing abundant silanol nests, are often called defective zeolites. In addition to weak acidity, silanol nests can also provide active sites and space for grafting other atoms.[45] There are a large number of silanol nests in P-D. As shown in IR spectra in the fingerprint of hydroxyl group (**Fig. 4b**), we observe six vibrational bands, assignments of which are summarized in **Table 3**. For E-D, the intensity of 3741 cm^{-1} is clearly increased with the additional of SiO_2 binders, while those for E-D-2.1%T and E-D-2.1%T-Al are reduced. Such difference indicates that SiO_2 binders convert into zeolite structure in E-D, which is in line with XRD results. Moreover, the band at 3450 cm^{-1} disappears for E-D-2.1%T-Al, which can be explained that the aluminum atoms fill up all of the silanol nests.

The use of pyridine and 2,6-di-tert-butylpyridine adsorption as probe molecules is adequate to investigate the internal and external surface acid amount, respectively. As shown in **Fig. 4c**, the peaks at 1540 cm^{-1} and 1450 cm^{-1} belong to Brønsted acid and Lewis acid sites, respectively.[39] As can be seen in **Fig. 4d**, the peak at 1633 cm^{-1} belongs to Brønsted acid sites on the external surface.[46] For E-D, the intensity of 1540 cm^{-1} is clearly reduced, which is attributed to the diluted acid sites caused by binder. Besides, E-D displays the largest 2,6-di-tert-butylpyridine adsorption peak due to the migration of framework Al atoms to surface. For E-D-2.1%T, the acid amount of Brønsted acid decreases while that of Lewis acid increases. Considering the decrease in the amount of Brønsted acid on the external surface, we can infer that the position of aluminum is redistributed during the TPAOH treatment. For E-D-2.1%T-Al, the amount of Brønsted acidic sites is increased compared with that for E-D, resulting from the transformation of additional aluminum sources into Al sites in the framework.

distributions of Si(nAl) units. However, the signal of $SiOH(SiO)_3$ group is commonly indistinct and overlaps with that of Si(1Al). With CP technique, the signals of silicon atoms bearing OH groups (SiOH) can be enhanced significantly, although the CP spectra are not quantitatively reliable. **Fig. 4f** presents $^1H \rightarrow ^{29}Si$ CP MAS NMR spectra of different samples. In ^{29}Si NMR, Q^3/Q^4 ratios decrease in the sequence of E-D＞E-D-2.1%T＞E-D-2.1%T-Al, which can corroborate the conversion of binder particles into crystallized zeolites frameworks and the incorporation of Al atoms into zeolite framework sites which through the reaction of aluminum halides with silanol nests. E-D can be regarded as the mechanical mixture of ZSM-5 powder and silica binder, and a part of Si atoms are supplied by silica binder. It possesses a higher Q^3/Q^4 ratio because of its low condensation degree of Si-OH bond in frameworks. However, E-D-2.1%T and E-D-2.1%T-Al are quite different from its precursor, namely E-D, yet they are similar to P-D. This possibly stems from the gradual formation of Si–O–Si bond that condenses from Si-OH groups

Table 4 Properties of the different ZSM-5 zeolites

Samples	N_2-adsorption results					Crushing strength[d] (N·cm^{-1})
	V_{tol}[a] ($cm^3\ g^{-1}$)	V_{micro}[b] ($cm^3\ g^{-1}$)	S_{BET}[c] ($cm^3\ g^{-1}$)	S_{micro}[b] ($m^2\ g^{-1}$)	S_{meso}[b] ($m^2\ g^{-1}$)	
P-D	0.22	0.11	386	261	125	—
E-D	0.24	0.09	348	207	141	28.3
E-D-0.6%T	0.22	0.10	375	220	155	33.3
E-D-0.6%T-Al	0.20	0.10	377	215	162	30.3
E-D-2.1%T	0.23	0.10	403	226	177	40.7
E-D-2.1%T-Al	0.23	0.10	407	230	177	32.7
P-C	0.22	0.14	410	318	92	—
E-C	0.26	0.11	380	248	132	29.5
E-C-2.1%T	0.25	0.12	382	286	96	39.0
E-C-2.1%T-Al	0.26	0.14	351	246	105	35.2

[a] V_{total} was determined from the amount of N_2 adsorbed at $p/p_0 = 0.99$

[b] *t*-plot method applied to the N_2 isotherm

[c] BET method applied to the N_2 isotherm

[d] Average value of 20 single particles

As shown in **Fig. 4e**, ^{27}Al MAS NMR is used to characterize the distortion of aluminum sites. A single signal at 54 ppm is assigned to four-coordinated framework Al, and another signal at 0 ppm is attributed to six-coordinated extraframework Al.[47] E-D-2.1%T-Al presents weak signal at 0 ppm, indicative of the existence of less extraframework Al. XPS results show a lower surface SiO_2/Al_2O_3 molar ratio of E-D-2.1%T-Al than those of other samples (**Table S7**), implying that a part of Al atoms exists on the external surface of zeolite. Besides, ICP-OES results (**Table S8**) confirm that a trace amount of Al atoms exists in the filtrate of TPAOH. Combining the above results, we can state that most of the aluminum sources are transformed into framework Al sites.

To further confirm the conversion of silica binders and the additional aluminum source into zeolite framework, we introduced the $^1H \rightarrow ^{29}Si$ cross-polarization (CP) MAS NMR technique. Generally, ^{29}Si MAS NMR is used for zeolites to establish the relative in re-crystallization.

3.2 Differences between defective ZSM-5 zeolites and commercial ZSM-5 zeolites

Fig. 5 shows N_2 adsorption-desorption isotherms and pore size distributions of different defective samples. The isotherms of P-D, E-D-0.6%T, and E-D-0.6%T-Al are identified as Type I, which is characteristic of micro-porosity and limited meso-porosity. On the other hand, the isotherm of E-D is identified as a combination of Type I and Type IV with H1 hysteresis loop, indicating the presence of mesopores. Nevertheless, this formation of additional mesopores mainly comes from the staking effect of silica binder, because the meso-porosity in P-D is insignificant. Moreover, the N_2 sorption on E-D-2.1%T and E-D-2.1%T-Al possesses a typical Type-IV isotherm, indicating the existence of mesopores. **Table 4** lists the surface area of mesopore which increases from 125 to 177 $m^2\ g^{-1}$. The pore size distributions of P-D, E-D-0.6%T, and E-D-0.6%T-Al show limited

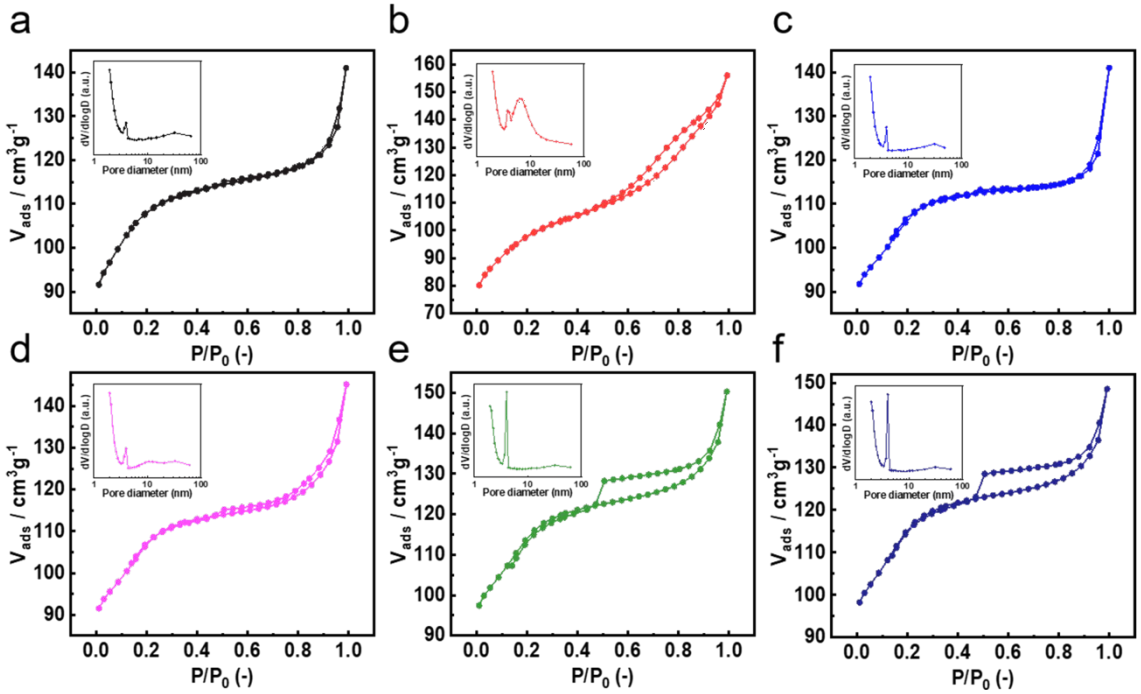

Fig. 5 N_2-adsorption and desorption isotherms of the different defective ZSM-5 zeolites.
(a) P-D (defective ZSM-5 zeolite powder), (b) E-D (Extrudate: P-D + 20% SiO_2 binder), (c) E-D-0.6%T (0.6%TPAOH treatment of E-D), (d) E-D-0.6%T-Al (E-D-0.6%T + 0.03 g Al_2O_3), (e) E-D-2.1%T (2.1%TPAOH treatment of E-D), (f) E-D-2.1%T-Al (E-D-2.1%T+ 0.03 g Al_2O_3).

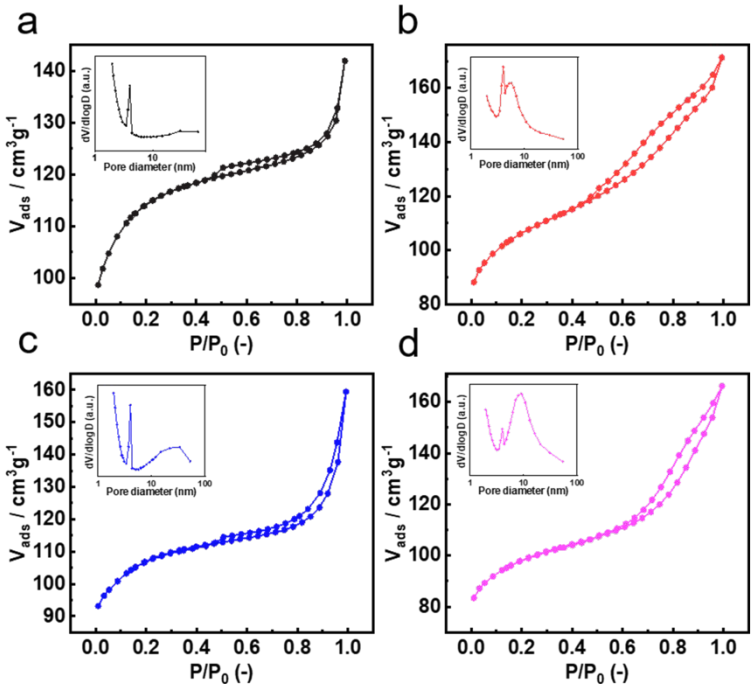

Fig. 6 N_2-adsorption and desorption isotherms of the different commercial ZSM-5 zeolites.
(a) P-C (commercial ZSM-5 zeolite powder), (b) E-C (Extrudate: P-C + 20% SiO_2 binder), (c) E-C-2.1%T (2.1%TPAOH treatment of E-C), (d) E-C-2.1%T-Al (E-C-2.1%T + 0.03 g Al_2O_3).

meso-pores volumes are mainly located at the pore size of 4 nm. Besides, E-D shows the formation of meso-pore volumes at the pore size of 4 nm and 6 nm, which are contributed to MFI zeolites and the binders, respectively. The only sharp distribution of the mesopores around 4 nm in E-D-2.1%T and E-D-2.1%T-Al suggests that binders are converted into the zeolite phase.

Fig. 6 exhibits the N_2 adsorption-desorption isotherms and pore size distributions of the same commercial samples. The isotherm of P-C is Type I with micropore and limited mesopore. The isotherm of E-C resembles that of E-D. For E-C-2.1%T, the total BET surface area is increased, resulting from the alkali treatment-induced conversion of most binders into zeolite phase (**Table 4**). Differently, E-C-2.1%T-

Al exhibits a similar isotherm as E-C, which is due to unsuccessful conversion of binders into zeolite.

Fig. 7 HAADF-STEM images of the different defective ZSM-5 zeolites. (a) P-D (defective ZSM-5 zeolite powder), (b) E-D (Extrudate: P-D + 20% SiO_2 binder), (c) E-D-0.6%T (0.6%TPAOH treatment of E-D), (d) E-D-0.6%T-Al (E-D-0.6%T + 0.03 g Al_2O_3), (e) E-D-2.1%T (2.1%TPAOH treatment of E-D), (f) E-D-2.1%T-Al (E-D-2.1%T+ 0.03 g Al_2O_3).

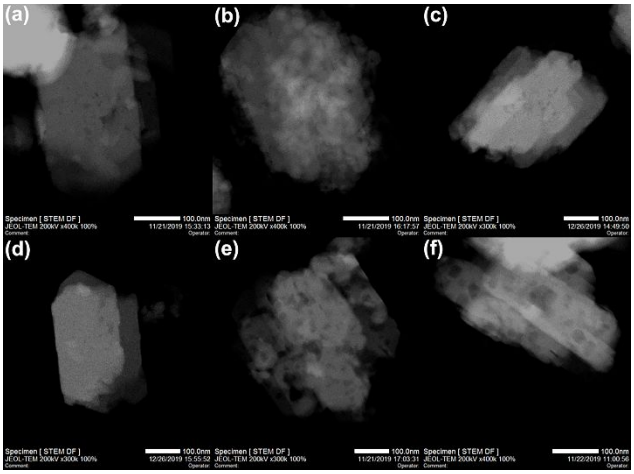

HAADF-STEM and TEM images are shown in **Fig. 7** and **8**, respectively. As shown in **Fig. 7b** and **8b**, E-D presents two separated phases, namely zeolite phase and binder phase. For E-D-2.1%T and E-D-2.1%T-Al (**Fig. 7e**, **8e** and **7f**, **8f**, respectively), they show a uniform zeolite phase with mesoporous structures, corroborating that SiO_2 binders are converted into MFI structure. Similar phenomena are also observed on E-D-0.6%T and E-D-0.6%T-Al (**Fig. 7c**, **8c** and **7d**, **8d**, respectively). The only difference is that E-D-0.6%T and E-D-0.6%T-Al are mainly composed of micropores. This is because the alkali concentration of TPAOH treatment is too low to etch away the mesopores. Crushing strength is also measured on each sample by testing 20 particles with radial grain crushing, as listed in **Table 4**. Clearly, the average crushing strength value increases after re-crystallization. More closed inter-crystal interaction and regular arrangement of crystals should account for the strengthened mechanical strength. Undoubtedly, the improvement of its mechanical properties of hierarchical zeolites is of great significance in terms of practical applications.

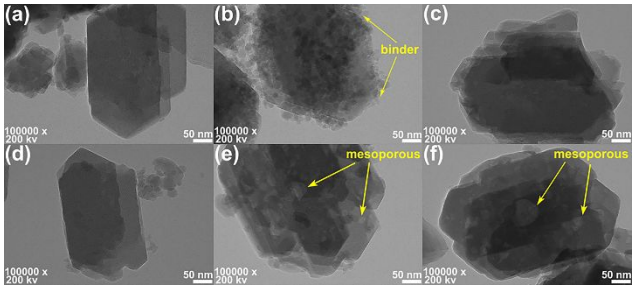

Fig. 8 TEM images of the different defective ZSM-5 zeolites. (a) P-D (defective ZSM-5 zeolite powder), (b) E-D (Extrudate: P-D + 20% SiO_2 binder), (c) E-D-0.6%T (0.6%TPAOH treatment of E-D), (d) E-D-0.6%T-Al (E-D-0.6%T + 0.03 g Al_2O_3), (e) E-D-2.1%T (2.1%TPAOH treatment of E-D), (f) E-D-2.1%T-Al (E-D-2.1%T + 0.03 g Al_2O_3).

Fig. 9a shows IR spectra in the fingerprint of hydroxyl group of different commercial ZSM-5 zeolites. There are three main bands, the assignments of which are shown in **Table 3**. Clearly, no absorption peaks are evident in the region of 3200~3500 cm^{-1}, confirming the absence of silanol nests in those four commercial ZSM-5 zeolites. **Fig. 9b** also displays TEM images of the same commercial samples. E-C presents two separated phases including zeolite phase and binder phase. E-C-2.1%T exhibits a more distinct zeolite phase with less unconverted binder particles. By contrast, E-C-2.1%T-Al composes of two separate phases, namely binder particles and zeolite crystals. This implies that most binders are not converted into zeolite phases. The additional aluminum source may form an aluminum shell on the zeolite surface and inhibit re-crystallization.

3.3 Proposed formation mechanisms of binderless zeolite

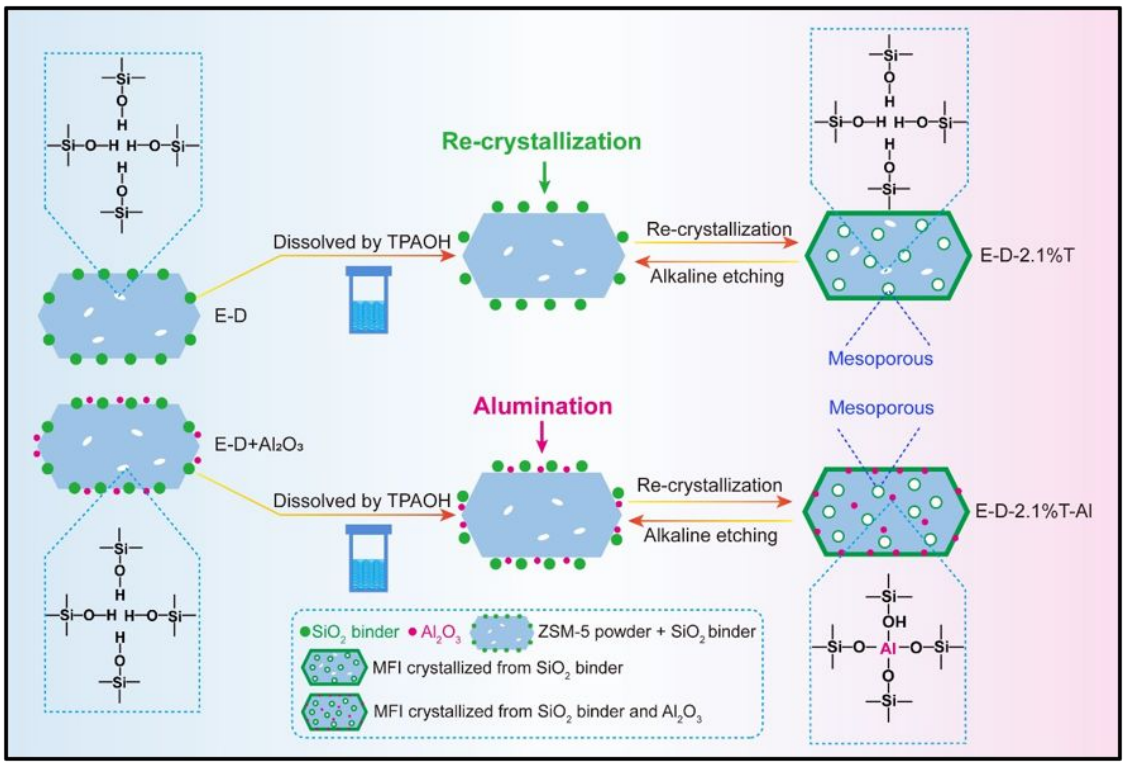

Scheme 1 Re-crystallization and alumination process of the defective ZSM-5 zeolites.

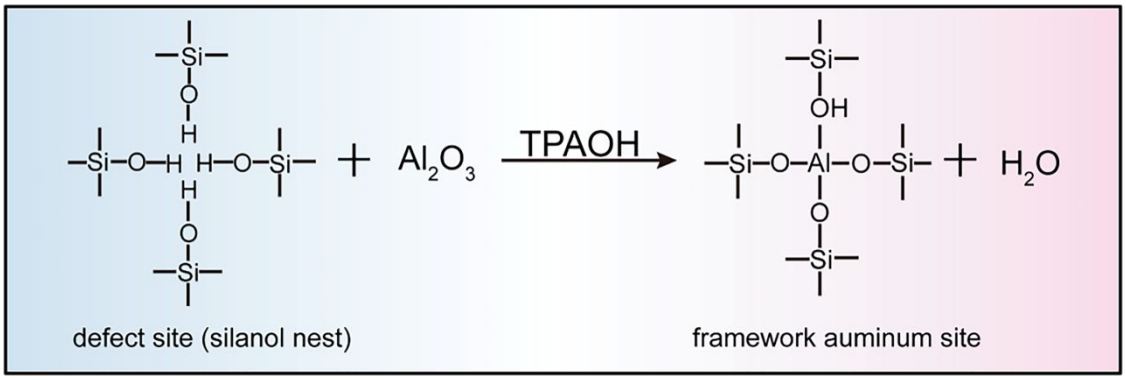

Scheme 2 Local structure of vacancies consisting of a silanol nest and their variation by the introduction of aluminum source.

According to the characterization results above, formation mechanisms of binderless zeolite are proposed and demonstrated in **Scheme 1**. Initially, the binder particles are easily dissolved in TPAOH solutions. Subsequently, zeolite crystals gradually grow up in partial, during which the dissolved species of binders is used as raw materials. Meanwhile, TPAOH solution helps etch away mesopores in zeolite crystals, which is known as desilication-recrystallization process.[48] The re-crystallization and alkaline etching are in dynamic balance. To better explain the formation mechanisms of binderless zeolite, we track the time of TPAOH treatment to give out the detailed changes of acidity, hydroxyl-nest defect and pore structure. As shown in Fig. S3 and Table S9, we can find that the time of TPAOH treatment has little effect on the hydroxyl-nest of the binderless zeolite, and the mesopore surface area is increased with the prolonged TPAOH-treatment time. However, the acidity of the binderless catalyst changes dynamically with the increase of treatment time.

In our study, it is found that the binder can be converted into zeolite phase in the re-crystallization process, but the acidity of the catalysts decreases significantly. To recover the acidity of the binderless catalyst the defective ZSM-5 zeolite was used as the raw material, and additional aluminum source was added during the re-crystallization process. This is known as alumination (**Scheme 1**).[49] According to NH_3-TPD, Py-IR, and OH-IR results, the mechanism of alumination process is further proposed in **Scheme 2**. The aluminum atoms are inserted into the framework through the reaction between Al_2O_3 and silanol nests. The amount of framework aluminum increases upon the alumination and mainly depends on the number of defect sites,

namely silanol nests. To verify this assumption, we explored the influence of different amounts of aluminum on alumination process. As shown in **Fig. 10**, the acid sites are maximized under the alumination condition of adding 0.03 g Al_2O_3, rather than at the 0.01 g or 0.05 g Al_2O_3. Besides, there is no signal at 3450 cm^{-1} in OH-IR spectrum for E-D-2.1%T-Al (**Fig. 4b**); meanwhile, the amount of Brønsted acidic sites is clearly increased for E-D-2.1%T-Al (**Fig. 4c**). The results show that the aluminum atoms fill up all silanol nests under the alumination condition of adding 0.03 g Al_2O_3. 0.01 g Al_2O_3 couldn't fill up all silanol nests as the insufficient amount of aluminum, and 0.05 g Al_2O_3 will deposit on the zeolite after filling up all silanol nests, which will reduce its acidity.

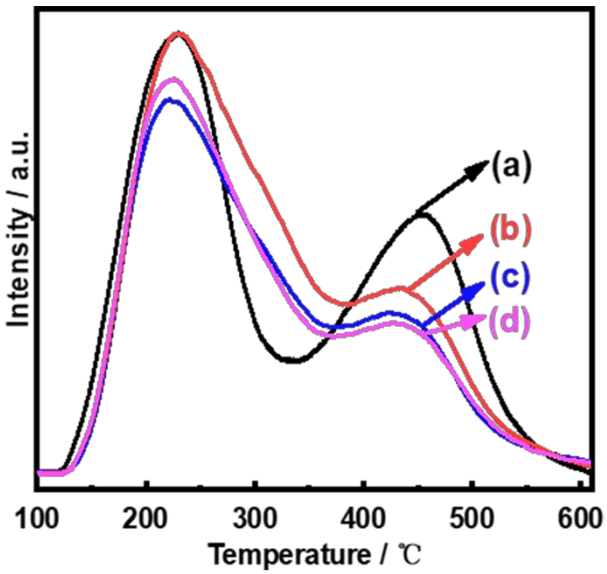

Fig. 10 NH_3-TPD profiles of the effect over different amounts of aluminum source on the acidity of different defective ZSM-5 zeolites during alumination process.
(a) P-D (defective ZSM-5 zeolite powder), (b) E-D-2.1%T-Al (E-D-2.1%T + 0.03 g Al_2O_3), (c) E-D-2.1%T-Al-1 (E-D-2.1%T + 0.01 g Al_2O_3), (d) E-D-2.1%T-Al-2 (E-D-2.1%T + 0.05 g Al_2O_3).

To further clarify the effect of silanol nests, the commercial ZSM-5 zeolites in the absence of defect sites (silanol nests) were used for comparison and treated in the same way as the defective samples. As shown in TEM images, there are still a lot of SiO_2 binders on the surface of the zeolite (**Fig. 9b**). Thus, it can be concluded that due to the absence of defective sites (silanol nests), the additional aluminum source cannot enter zeolite framework; instead, it deposits on the surface of zeolite and inhibits re-crystallization. These facts strongly support the former statement that Al atoms are incorporated into the defect sites by the reaction between Al_2O_3 with the silanol nests.

3.4 Performance in *n*-hexane catalytic cracking reaction

Catalytic cracking of light alkanes such as *n*-hexane is of considerable significance, because it produces light olefins such as ethylene and propylene which are important commodity in petrochemistry.[50] ZSM-5 zeolite, with the MFI structure, has been widely used in the context of catalytic cracking due to its strong acidity and high hydrothermal stabilities. It is well accepted that the activity of *n*-hexane catalytic cracking mainly depends on the acidity of the catalyst.[51, 52]

The catalytic cracking of *n*-hexane was carried out over as-prepared catalysts at various reaction temperatures. The *n*-hexane conversion rates as a function of temperature are plotted in **Fig. 11a**. The conversion of *n*-hexane increases with the temperature for all catalysts. For E-D-2.1%T-Al, its *n*-hexane conversion is higher than that for E-D, but lower than that for P-D. This demonstrates that additional aluminum sources successfully transform into framework Al sites in E-D-2.1%T-Al, through which the acidity of E-D-2.1%T-Al is partially restored. The product distribution is also compared in **Fig. 11b** and **Table S10**. For most catalysts, the selectivity of C_2-$C_3^=$ olefins increase along with the reaction temperature, and the selectivity for BTX (benzene, toluene, and xylene) is not much different. **Fig. S4** shows a clear linear relationship between micropores, the amount of Brønsted acid, and *n*-hexane conversion. This indicates that the catalytic cracking of *n*-hexane is mainly related to the Brønsted acid in the micropore. The result shows that adding aluminum source during alkaline treatment can increase the acidity of monolithic catalysts, making them potential catalyst candidate for cracking of light alkanes.

4. Conclusions

In summary, two kinds of shaped structured binderless ZSM-5 catalysts are prepared by the alkali treatment method: the monolithic binderless ZSM-5 zeolites dominated by micropores and the hierarchical monolithic binderless ZSM-5 zeolites. Our results

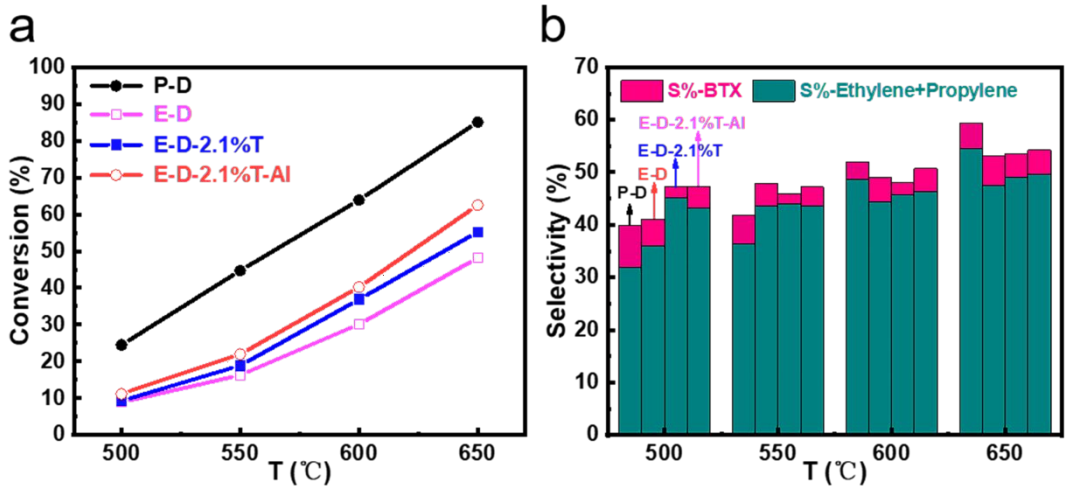

Fig. 11 Catalytic performance of the different defective ZSM-5 zeolites in the *n*-hexane catalytic cracking reaction on P-D (defective ZSM-5 zeolite powder), E-D (Extrudate: P-D + 20% SiO_2 binder), E-D-2.1%T (2.1%TPAOH treatment of E-D), and E-D-2.1%T-Al (E-D-2.1%T+ 0.03 g Al_2O_3).
(a) *n*-Hexane conversion over different defective ZSM-5 zeolites. (b) Products selectivity over different defective ZSM-5 zeolites.

demonstrate that post-treatments of binderless monolithic zeolites via re-crystallization and alumination process are advantageous in three major aspects from practical point of view: 1) SiO_2 binders convert into the zeolite phase to solve the binder-covering issue; 2) the mechanical strength of binderless zeolites is significantly increased in comparison to that of shaped catalyst; 3) the acidity of the binderless defective ZSM-5 zeolite is appreciably increased through alumination during alkali treatment. Of note, choosing defective zeolite is a prerequisite, as the aluminum source can react with the silanol nest, through which Al can migrate into zeolite framework. Therefore, the binderless defective zeolite with strengthened acidity demonstrates higher activity and selectivity than the ordinary shaped zeolite with a binder in the acidity-determined *n*-hexane catalytic cracking reaction. This work provides new insight into the contribution of fundamentals in optimizing existing zeolite catalysts.

Conflicts of interest

There are no conflicts to declare.

Acknowledgements

The authors (J.L. and J.L) acknowledges the financial supports from the Fundamental Research Funds for the Central Universities (DUT20LAB127). X.J. acknowledges the financial support from the Center for Understanding the Control of Acid Gas-Induced Evolution of Materials for Energy (UNCAGE-ME), an Energy Frontier Research Center funded by U.S. Department of Energy, Office of Science, Basic Energy Sciences.

Notes and references

1. A. Corma, *Chem. Rev.*, 1997, **97**, 2373-2420.
2. C. S. Cundy and P. A. Cox, *Chem. Rev.*, 2003, **103**, 663-702.
3. A. Corma, *J. Catal.*, 2003, **216**, 298-312.
4. J. Čejka and S. Mintova, *Catal. Rev.*, 2007, **49**, 457-509.
5. X. Meng, F. Nawaz and F.-S. Xiao, *Nano Today*, 2009, **4**, 292-301.
6. S. Mitchell, N.-L. Michels and J. Pérez-Ramírez, *Chem. Soc. Rev.*, 2013, **42**, 6094-6112.
7. J. S. Beck, J. C. Vartuli, W. J. Roth, M. E. Leonowicz, C. T. Kresge, K. D. Schmitt, C. T. W. Chu, D. H. Olson, E. W. Sheppard, S. B. McCullen, J. B. Higgins and J. L. Schlenker, *J. Am. Chem. Soc.*, 1992, **114**, 10834-10843.
8. D. Gao, A. Duan, X. Zhang, K. Chi, Z. Zhao, J. Li, Y. Qin, X. Wang and C. Xu, *J. Mater. Chem. A*, 2015, **3**, 16501-16512.
9. D. H. Park, S. S. Kim, H. Wang, T. J. Pinnavaia, M. C. Papapetrou, A. A. Lappas and K. S. Triantafyllidis, *Angew. Chem., Int. Ed.*, 2009, **48**, 7645-7648.
10. A. Karlsson, M. Stöcker and R. Schmidt, *Microporous Mesoporous Mater.*, 1999, **27**, 181-192.
11. M. Hartmann, *Angew. Chem., Int. Ed.*, 2004, **43**, 5880-5882.
12. J. C. Groen, J. A. Moulijn and J. Pérez-Ramírez, *Microporous Mesoporous Mater.*, 2005, **87**, 153-161.
13. W. Fan, M. A. Snyder, S. Kumar, P.-S. Lee, W. C. Yoo, A. V. McCormick, R. Lee Penn, A. Stein and M. Tsapatsis, *Nat. Mater.*, 2008, **7**, 984-991.
14. M. Mańko, J. Vittenet, J. Rodriguez, D. Cot, J. Mendret, S. Brosillon, W. Makowski and A. Galarneau, *Microporous Mesoporous Mater.*, 2013, **176**, 145-154.
15. J. Pérez-Ramírez, S. Mitchell, D. Verboekend, M. Milina, N.-L. Michels, F. Krumeich, N. Marti and M. Erdmann, *ChemCatChem*, 2011, **3**, 1731-1734.
16. S. Mitchell, N.-L. Michels, K. Kunze and J. Pérez-Ramírez, *Nat. Chem.*, 2012, **4**, 825-831.
17. Z. Shen, C. Ma, J. He, D. Wang, H. Sun, Z. Zhu and W. Yang, *Appl. Catal., A*, 2019, **577**, 20-27.
18. Y. Didi, B. Said, T. Cacciaguerra, K. L. Nguyen, V. Wernert, R. Denoyel, D. Cot, W. Sebai, M.-P. Belleville, J. Sanchez-Marcano, F. Fajula and A. Galarneau, *Microporous Mesoporous Mater.*, 2019, **281**, 57-65.
19. J. E. Antia, K. Israni and R. Govind, *Appl. Catal., A*, 1997, **159**, 89-99.
20. N.-L. Michels, S. Mitchell and J. Pérez-Ramírez, *ACS Catal.*, 2014, **4**, 2409-2417.
21. G. T. Whiting, F. Meirer, M. M. Mertens, A.-J. Bons, B. M. Weiss, P. A. Stevens, E. de Smit and B. M. Weckhuysen, *ChemCatChem*, 2015, **7**, 1312-1321.
22. G. T. Whiting, A. D. Chowdhury, R. Oord, P. Paalanen and B. M. Weckhuysen, *Faraday Discuss.*, 2016, **188**, 369-386.
23. G. T. Whiting, S.-H. Chung, D. Stosic, A. D. Chowdhury, L. I. van der Wal, D. Fu, J. Zecevic, A. Travert, K. Houben, M. Baldus and B. M. Weckhuysen, *ACS Catal.*, 2019, **9**, 4792-4803.
24. J. S. J. Hargreaves and A. L. Munnoch, *Catal. Sci. Technol.*, 2013, **3**, 1165-1171.
25. J. Wang, X. Cheng, J. Guo, X. Chen, H. He and Y. Long, *Chin. J. Chem.*, 2010, **28**, 183-188.
26. J. Zhou, J. Teng, L. Ren, Y. Wang, Z. Liu, W. Liu, W. Yang and Z. Xie, *J. Catal.*, 2016, **340**, 166-176.
27. F. Scheffler, W. Schwieger, D. Freude, H. Liu, W. Heyer and F. Janowski, *Microporous Mesoporous Mater.*, 2002, **55**, 181-191.
28. P. R. H. P. Rao and M. Matsukata, *Chem. Commun.*, 1996, DOI: 10.1039/CC9960001441, 1441-1442.
29. A. Özcan and H. Kalıpçılar, *Ind. Eng. Chem. Res.*, 2006, **45**, 4977-4984.
30. M. Matsukata, N. Nishiyama and K. Ueyama, *Microporous Mater.*, 1993, **1**, 219-222.
31. B. Louis, F. Ocampo, H. S. Yun, J. P. Tessonnier and M. M. Pereira, *Chem. Eng. J.*, 2010, **161**, 397-402.
32. T. Hu, J. Liu, C. Cao and W. Song, *Chin. J. Catal.*, 2017, **38**, 872-877.
33. G. Guo and Y. Long, *Sep. Purif. Technol.*, 2001, **24**, 507-518.
34. T. Fakin, A. Ristić, V. Mavrodinova and N. Zabukovec Logar, *Microporous Mesoporous Mater.*, 2015, **213**, 108-117.
35. A. Arefi Pour, S. Sharifnia, R. Neishabori Salehi and M. Ghodrati, *J. Nat. Gas Sci. Eng.*, 2016, **36**, 630-643.
36. R. M. Barrer and M. B. Makki, *Can. J. Chem.*, 1964, **42**, 1481-1487.

37. C. D. Chang, C. T. W. Chu, J. N. Miale, R. F. Bridger and R. B. Calvert, *J. Am. Chem. Soc.*, 1984, **106**, 8143-8146.
38. L. Lin, X. Zhang, N. He, J. Liu, Q. Xin and H. Guo, *Catalysts*, 2019, **9**, 100.
39. C. A. Emeis, *J. Catal.*, 1993, **141**, 347-354.
40. F. Lonyi, J. Valyon, Micro. Meso. Material 2001, 47, 293-301.
41. L. R. Gonzalez, F. Hermes, M. Bertmer, E. R. Castellon, A. J. Lopez, U. Simon, Appl. Catal., A 2007, 328, 174-182.
42. E. Janiszewska, J. Kowalska-Kuś, K. Góra-Marek, A. Szymocha, K. Nowińska and S. Kowalak, *Appl. Catal., A*, 2019, **581**, 1-10.
43. P. Wu, T. Komatsu and T. Yashima, *J. Phys. Chem.*, 1995, **99**, 10923-10931.
44. K. Barbera, F. Bonino, S. Bordiga, T. V. W. Janssens and P. Beato, *J. Catal.*, 2011, **280**, 196-205.
45. W. N. P. van der Graaff, G. Li, B. Mezari, E. A. Pidko and E. J. M. Hensen, *ChemCatChem*, 2015, **7**, 1152-1160.
46. A. Corma, V. Fornés, L. Forni, F. Márquez, J. Martínez-Triguero and D. Moscotti, *J. Catal.*, 1998, **179**, 451-458.
47. R. Zhao, Z. Zhao, S. Li and W. Zhang, *J. Phys. Chem. Lett.*, 2017, **8**, 2323-2327.
48. J. Pérez-Ramírez, C. H. Christensen, K. Egeblad, C. H. Christensen and J. C. Groen, *Chem. Soc. Rev.*, 2008, **37**, 2530-2542.
49. K. Yamagishi, S. Namba and T. Yashima, *J. Phys. Chem.*, 1991, **95**, 872-877.
50. K. Kubo, H. Iida, S. Namba and A. Igarashi, *Microporous Mesoporous Mater.*, 2012, **149**, 126-133.
51. S. T. Sie, *Ind. Eng. Chem. Res.*, 1992, **31**, 1881-1889.
52. X. Li, W. Li, F. Rezaei and A. Rownaghi, *Chem. Eng. J.*, 2018, **333**, 545-553.

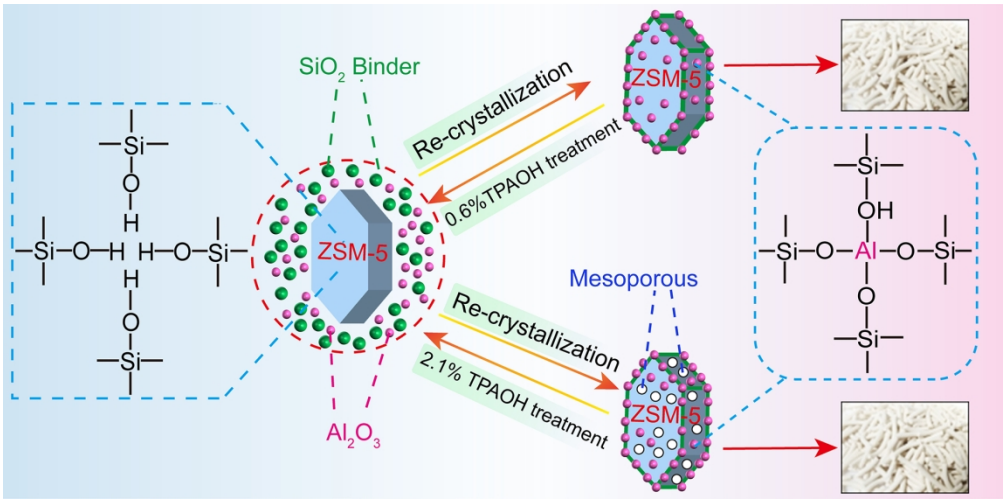
SiO2 Binder
ZSM-5
Al2O3
Re-crystallization
0.6%TPAOH treatment
ZSM-5
Mesoporous
Re-crystallization
2.1% TPAOH treatment
ZSM-5
Si
O
H
OH
Al